Bricked subwavelength gratings: a tailorable on-chip metamaterial topology

Luque-González, José Manuel; Ortega-Moñux, Alejandro; Halir, Robert; Schmid, Jens H.; Cheben, Pavel; Molina-Fernández, Íñigo; Wangüemert-Pérez, J. Gonzalo

Publisher's version / Version de l'éditeur:
https://doi.org/10.1002/lpor.202000478
Laser & Photonics Reviews, 15, 6, 2021-05-02

Bricked Subwavelength Gratings: A Tailorable On-Chip Metamaterial Topology

José Manuel Luque-González, Alejandro Ortega-Moñux, Robert Halir, Jens H. Schmid, Pavel Cheben, Íñigo Molina-Fernández, and J. Gonzalo Wangüemert-Pérez*

Integrated metamaterials are redefining the capabilities of silicon photonic chips. In providing lithographic control over dielectric permittivity, dispersion and anisotropy, they are enabling photonic devices with unprecedented performance. However, the implementation of these materials at telecom wavelengths often requires a fabrication resolution of the order of 100 nm and below, pushing current wafer-scale fabrication technology to its limits and hindering the widespread exploitation of on-chip metamaterials. Herein, a subwavelength grating metamaterial with bricked topology is proposed, that provides lithographic control over the metamaterial dispersion and anisotropy using a single etch Manhattan-like geometry with pixel dimensions up to 150 × 150 nm^2, thereby easing the path toward fabrication at wafer-scale. The behavior of these structures as biaxial crystals is analytically shown, validating their use in high performance on-chip beam-splitters. Through engineering of the metamaterial anisotropy tensor, the splitters are shown to exhibit sub-decibel insertion losses and imbalance over a 400 nm design bandwidth, via 3D FDTD simulations. The excellent device performance is demonstrated over a 140 nm bandwidth, limited by the measurement setup.

1. Introduction

Driven by high quality lithography and dense optical integration, silicon photonics is enabling key advances in diverse areas including high speed optical communications,[1] quantum technologies,[2,3] artificial intelligence,[4,5] supercomputing,[6,7] lidars,[8] spectroscopy[9] or sensing.[10] For these developments, preserving CMOS compatibility is crucial in order to leverage existing microelectronics fabrication infrastructure to mass produce silicon photonic chips.[11,12] Since there are only a few fully CMOS compatible materials, the design space is largely restricted in terms of the available optical properties, and this ultimately limits device performance. Dielectric on-chip metamaterials, originally introduced to address the light coupling bottleneck in silicon photonics,[13,14] have the potential to overcome this limitation. By periodically patterning waveguides at the subwavelength scale, a wide range of equivalent refractive indexes can be synthesized lithographically on a chip.[15–18] What is more, with the ability to engineer dispersion and anisotropy these metamaterials are enabling completely new design strategies yielding devices with unprecedented performance, including ultra-broadband nanophotonic components,[19,20] metalenses,[21–23] densely spaced waveguides,[24] polarization management devices,[25–30] low crosstalk bends,[31] or high sensitivity waveguide sensors.[32,33] However, to avoid Bragg resonances, subwavelength grating (SWG) metamaterials often require fabrication resolutions of 100 nm and below at telecom wavelengths. While narrow single-mode SWG waveguides can operate with larger periods, for more sophisticated devices implemented in planar waveguides, the required resolutions can be prohibitively small to fabricate with wafer-scale lithography techniques. Advanced optical proximity correction techniques (OPC)[34] alleviate this issue for some device geometries. However, when control over material anisotropy is required, the structures that have so far been explored for this purpose (tilted, non-Manhattan patterns)[35] are not amenable to current OPC techniques. Therefore, exploiting the full potential of SWG metamaterials is challenging with current wafer-scale fabrication technologies, jeopardizing the broad use

J. M. Luque-González, Dr. A. Ortega-Moñux, Dr. R. Halir, Prof. Í. Molina-Fernández, Prof. J. G. Wangüemert-Pérez
Universidad de Málaga
Dept. de Ingeniería de Comunicaciones
ETSI Telecomunicación
Campus de Teatinos s/n
Málaga 29010, Spain
E-mail: jmlg@ic.uma.es

Dr. R. Halir, Prof. Í. Molina-Fernández
Bionand Center for Nanomedicine and Biotechnology
Parque Tecnológico de Andalucía
Málaga 29590, Spain

Dr. J. H. Schmid, Dr. P. Cheben
National Research Council Canada
1200 Montreal Road, Bldg. M50, Ottawa K1A 0R6, Canada

Dr. P. Cheben
Center for Research in Photonics
University of Ottawa
Ottawa K1N6N5, Canada

The ORCID identification number(s) for the author(s) of this article can be found under https://doi.org/10.1002/lpor.202000478

DOI: 10.1002/lpor.202000478

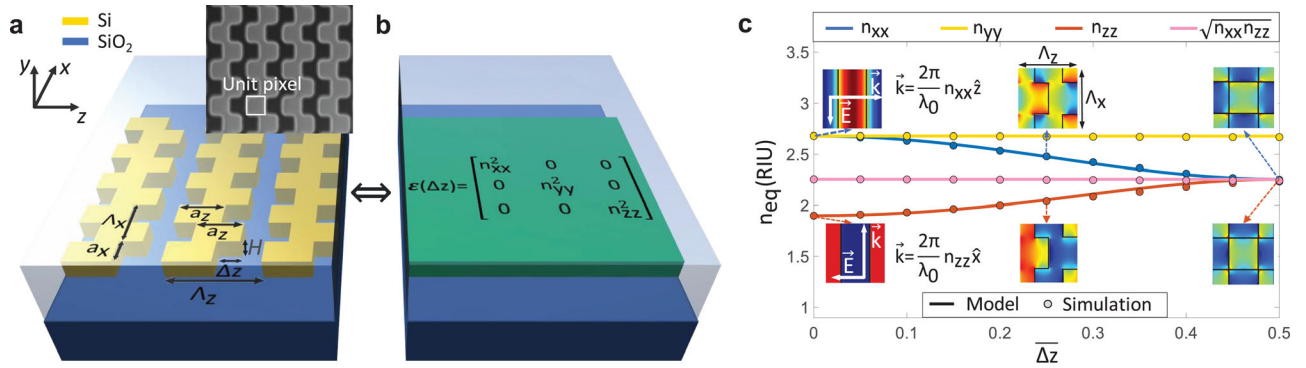

Figure 1. a) 3D-Schematic of a bricked SWG waveguide. The structure is formed by periodically partitioning the silicon segments of an SWG waveguide in the transverse direction (*x*-axis) alternately shifting the resulting blocks a length Δz. The silicon dioxide cladding is represented translucently. Inset: Scanning electron microscope (SEM) image of a fabricated bricked SWG structure, schematically showing a unit pixel. b) Anisotropic homogenization of the bricked SWG core shown in (a) as a metamaterial defined by its diagonal permittivity tensor $\varepsilon(\Delta z) = \mathrm{diag}[n_{xx}^2, n_{yy}^2, n_{zz}^2]$. c) The tensor components of the synthesized metamaterial are lithography tailored by the shift Δz, providing control over the properties of the synthesized metamaterial without changing the duty-cycle. The insets show the electric field distribution, for polarization along the *z*- and *x*-axis, propagating in the *x* and *z* directions, respectively, as the shifting is increased. The normalized shift is defined as $\overline{\Delta z} = \Delta z/\Lambda_z$.

of high-performance metamaterial designs in silicon photonic devices.

To overcome this limitation, here we propose the bricked subwavelength grating, shown in **Figure 1**a, a new nanopatterning for on-chip metamaterials, which synthesizes a tailorable biaxial crystal with lithographic control over anisotropy and dispersion. This is achieved with a single etch step Manhattan-like geometry with a uniform grid and pixel dimensions up to $150 \times 150\ \mathrm{nm}^2$ for telecom wavelengths, thereby paving the way toward wafer-scale fabrication. The control over the metamaterial optical properties enabled by bricked SWG opens a new design space in silicon photonics devices, especially in ultrabroadband devices with larger feature sizes and polarization management devices. We validate the dispersion control of bricked SWG metamaterials by designing on-chip beam-splitters with large pixel dimensions that cover bandwidths in excess of 400 nm at telecom wavelength with sub-decibel insertion losses and imbalance. These results are experimentally demonstrated in a 140 nm bandwidth, which is limited by the measurement setup.

2. Bricked SWG Metamaterials

2.1. Foundations of Bricked the SWG Metamaterial

A conventional subwavelength grating waveguide comprises alternating strips of the core and the cladding materials, arrayed with a subwavelength period Λ_z along the propagation direction (*z*-axis). Referring to Figure 1a, in a bricked SWG waveguide, the silicon strips are periodically partitioned along the *x*-axis with a pitch Λ_x, and the resulting silicon blocks are then alternately shifted by a distance Δz in the *z*-direction. We refer to the duty-cycles in the *x* and *z* directions as $\mathrm{DC}_x = a_x/\Lambda_x$ and $\mathrm{DC}_z = a_z/\Lambda_z$ respectively, setting them advantageously to 50% as this yields the largest pixel dimensions. To obtain an analytical model of this metamaterial we will consider a simplified structure that extends the bricked SWG medium infinitely along the *x*-axis and the *y*-axis, with light propagating in the *x*-*z* plane. For the purpose of illustration, we will consider a central wavelength of $\lambda_0 = 1.55\ \mu\mathrm{m}$, with material refractive indices $n_{\mathrm{Si}} = 3.476$ and $n_{\mathrm{SiO_2}} = 1.444$ and $\mathrm{DC}_x = \mathrm{DC}_z = 50\%$. At this point of the analysis we assume operation in the deep subwavelength regime, i.e., $\Lambda \ll \lambda_0$, as this simplifies the mathematical model – in the next section we show that the key predictions of this model remain valid for longer subwavelength periods. Based on our previous works,[19,22,35] we model the periodic structure as a homogeneous anisotropic medium, described by its permittivity tensor $\varepsilon(\overline{\Delta z})$

$$\varepsilon\left(\overline{\Delta z}\right) = \begin{bmatrix} n_{xx}^2\left(\overline{\Delta z}\right) & 0 \\ 0 & n_{zz}^2\left(\overline{\Delta z}\right) \end{bmatrix} \tag{1}$$

where $\overline{\Delta z} = \Delta z/\Lambda_z$. The n_{yy}^2 component of the permittivity tensor has been omitted because this component is independent of the block shifting, as will be demonstrated later in our analysis. We first consider the boundary case $\overline{\Delta z} = 0$, that is, a conventional SWG structure, for which the index tensor is given by: $n_{xx}(0) = n_{\parallel}$ and $n_{zz}(0) = n_{\perp}$, with $n_{\parallel}$ and $n_{\perp}$ being the equivalent refractive indices for polarization parallel and perpendicular to the interfaces between the interleaved materials. The permittivity tensor in this case is thus given by $\varepsilon(0) = \mathrm{diag}[n_{\parallel}^2, n_{\perp}^2]$. The constants $n_{\parallel}$ and $n_{\perp}$ can be analytically calculated using different approaches,[36,37] with the well-known Rytov formulas yielding $n_{\parallel} = [\mathrm{DC}_z n_{\mathrm{Si}}^2 + (1-\mathrm{DC}_z) n_{\mathrm{SiO_2}}^2]^{1/2} = 2.66$ and $n_{\perp} = [\mathrm{DC}_z n_{\mathrm{Si}}^{-2} + (1-\mathrm{DC}_z) n_{\mathrm{SiO_2}}^{-2}]^{-1/2} = 1.89$. Let's now consider a second a boundary case, $\overline{\Delta z} = 0.5$, yielding a chequerboard type structure – see insets in Figure 1c. Assuming a 50% duty cycle in both *x* and *z* directions, the symmetry of this configuration implies that light propagation is invariant along the *x* and *z* axes, that is, $n_{xx}(0.5) = n_{zz}(0.5)$. To calculate the component values in this case we use the index conservation law.[38] The latter implies that for a diagonal permittivity tensor the determinant,

$\det|\varepsilon(\overline{\Delta z})|$, is invariant on the shift $\overline{\Delta z}$, resulting in the following relation between the refractive index components

$$\det\left|\varepsilon\left(\overline{\Delta z}\right)\right| = n_{xx}^2\left(\overline{\Delta z}\right) n_{zz}^2\left(\overline{\Delta z}\right) = \det|\varepsilon(0)| = n_{\parallel}^2\, n_{\perp}^2 \tag{2}$$

Using this equation, we can calculate the permittivity tensor for the chequerboard geometry, obtaining $\epsilon(0.5) = \mathrm{diag}[n_{\perp}n_{\parallel}, n_{\perp}n_{\parallel}]$. So far, we have calculated the permittivity tensor for the boundary cases $\overline{\Delta z} = 0$, and $\overline{\Delta z} = 0.5$, directly from the symmetry considerations and the index conservation law. We now seek a periodical and smooth solution for the intermediate values of $\overline{\Delta z}$, assuming that $n_{xx}(\overline{\Delta z})$ can be expressed as

$$n_{xx}\left(\overline{\Delta z}\right) = A + B\cos\left(2\pi\overline{\Delta z}\right) \tag{3}$$

so that using Equation (2) the $n_{zz}(\overline{\Delta z})$ component is given by

$$n_{zz}\left(\overline{\Delta z}\right) = n_{\perp}\, n_{\parallel}\left[A + B\cos\left(2\pi\overline{\Delta z}\right)\right]^{-1} \tag{4}$$

with $A = 0.5(n_{\parallel} + \sqrt{n_{\parallel}n_{\perp}})$ and $B = 0.5(n_{\parallel} - \sqrt{n_{\parallel}n_{\perp}})$ obtained from the boundary cases $\overline{\Delta z} = 0$, and $\overline{\Delta z} = 0.5$. Figure 1c shows the calculated components of the tensor by using Equations (3) and (4) (solid lines). Simulation of the structure with a plane wave expansion tool[39] (Figure 1c, dots) shows an excellent agreement with the model – see the Supporting Information for further details on the simulation approach. The simulations also confirm that the n_{yy} component is not affected by the shifting, which can be intuitively understood by noting that the y-polarized electric field is always parallel to the interfaces.

We can draw several important conclusions from the results presented in Figure 1c. First, the bricked SWG effectively behaves as biaxial crystal, i.e., $n_{yy} \geq n_{xx} \geq n_{zz}$. Second, the properties of this crystal can be controlled by changing the shift Δz, while maintaining a rectangular, Manhattan-like geometry and constant duty-cycles. Third, for a x-polarized light wave propagating along the z-axis, the k-vector magnitude, $k(\overline{\Delta z}) = \frac{2\pi}{\lambda}\, n_{xx}(\overline{\Delta z})$, decreases as the shift is increased. This implies that compared to a conventional subwavelength grating, for a given period Λ_z, the Bragg resonance wavelength, $\lambda_B(\overline{\Delta z})$, is shortened

$$\lambda_B\left(\overline{\Delta z}\right) = 2\Lambda \cdot n_{xx}\left(\overline{\Delta z}\right) = \frac{\lambda_B(0)}{n_{xx}(0)}\, n_{xx}\left(\overline{\Delta z}\right) \tag{5}$$

In the next section we will show how Equation (5) accurately predicts the foreshortening of the Bragg wavelength not only in the infinitely extended metamaterial, but also when including mode confinement effect in a planar waveguide geometry.

2.2. Waveguiding in the Bricked SWG Metamaterial

We now examine the properties of bricked SWG metamaterials as the core of on-chip waveguides. We consider two waveguides both with a bricked SWG metamaterial core with $w = 3.3$ μm, a core thickness $H = 0.22$ μm and duty-cycles of 50% in both the x and z directions (i.e., yielding the largest pixel dimensions),

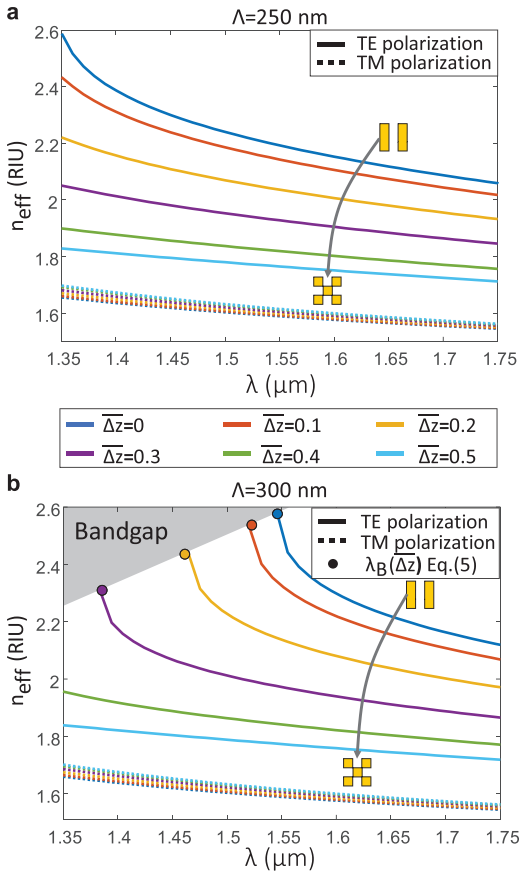

Figure 2. Effective index dispersion of the fundamental TE and TM Floquet-Bloch modes of a 220-nm-thick bricked SWG waveguide with a width $w = 3.3$ μm, a 50% duty cycle in both directions and with periods, Λ_x and Λ_z set to a) 250 nm b) 300 nm. As the shift is increased the bandgap moves to shorter wavelengths – equivalently, subwavelength operation is achieved with larger pixel dimensions. The Bragg wavelength predicted by using Equation (5) is shown with a dot for each shifting, achieving a simple but accurate approximation requiring only the simulation of the non-shifted topology. Furthermore, the modal birefringence can be precisely controlled: as the shift increases, the effective index of the fundamental TE mode is significantly reduced, while the fundamental TM mode is virtually unaffected.

with different periods. In the first waveguide the periods are set to $\Lambda_x = \Lambda_z = 250$ nm while in the second waveguide we choose $\Lambda_x = \Lambda_z = 300$ nm, so the Bragg wavelength is longer for the latter. In **Figure 2**a,b we show the effective index dispersion of the fundamental TE (x-polarized) and TM (y-polarized) Floquet-Bloch modes propagating along the z-axis, for different shifting values ranging from $\overline{\Delta z} = 0$ to $\overline{\Delta z} = 0.5$ for the $\Lambda = 250$ nm and $\Lambda = 300$ nm waveguides, respectively, calculated via 3D-FDTD simulations – see the Supporting Information for further details on the simulation approach. Simulation results plotted in Figure 2 clearly show that bricked SWG waveguides are highly polarization-dependent structures. The key point here is that the shifting provides an accurate control over the modal birefringence: the effective index and the dispersion of the fundamental TE mode (solid lines) are reduced as the shifting increases, while the fundamental TM mode (dotted lines) is almost unaffected.

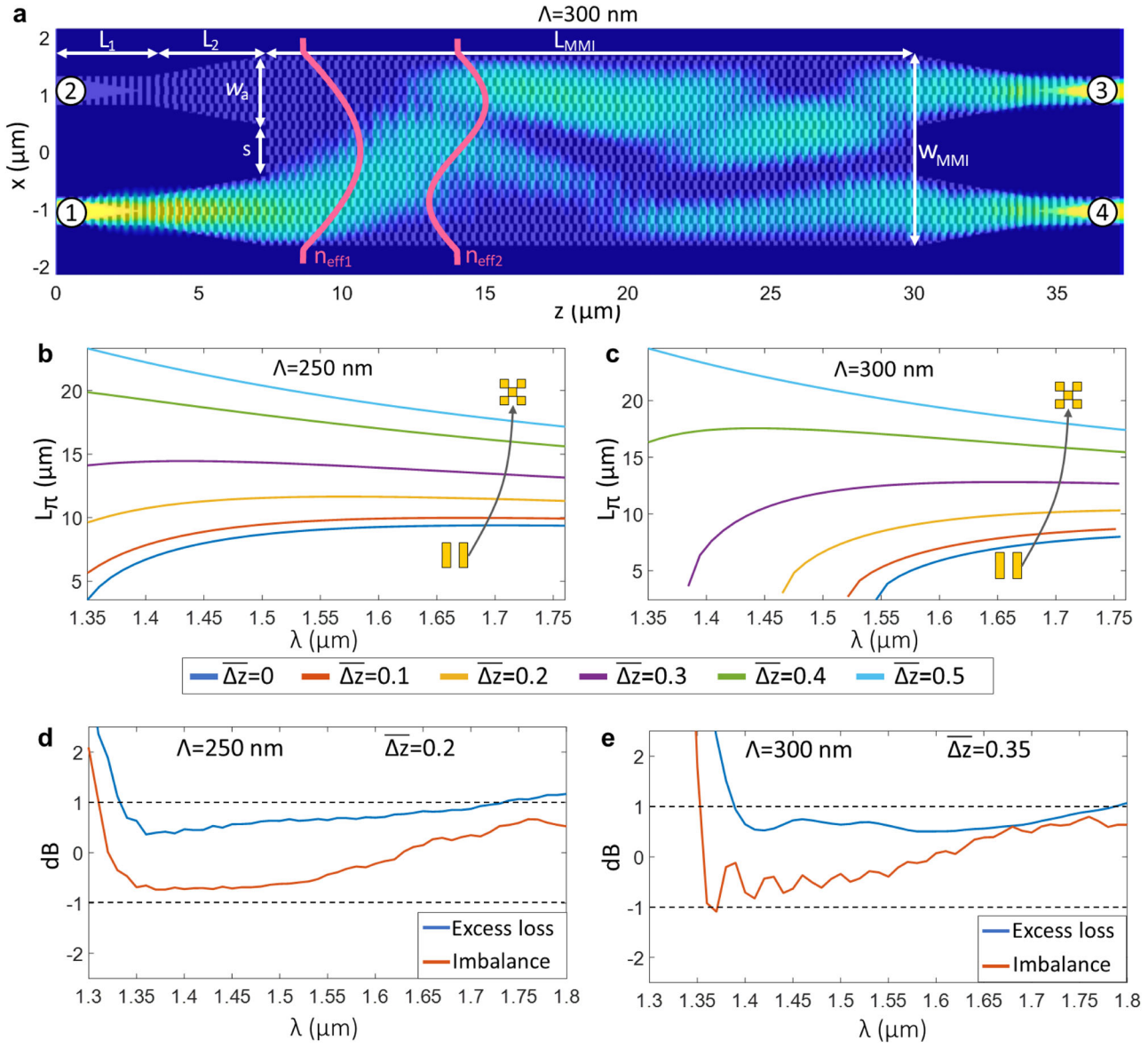

Figure 3. a) Simulated magnetic field propagation along the $\Lambda = 300$ nm bricked SWG based MMI design $|H_y|$. b,c) Fundamental and first order mode beat length dispersion of the TE polarization for the waveguide with (b), $\Lambda = 250$ nm and (c) $\Lambda = 300$ nm, with the shifting ranging from d,e) $\overline{\Delta z} = 0$ to $\overline{\Delta z} = 0.5$. Simulated excess loss (blue line) and imbalance (red line) of the optimized bricked SWG MMIs with a period of (d) $\Lambda = 250$ nm and (e) $\Lambda = 300$ nm. In both cases a 400 nm 1-dB-bandwidth is covered, from 1330 to 1730 nm (d), and from 1380 to 1780 nm (e).

The effect of the shift on the Bragg wavelength is particularly noticeable in Figure 2b. Without a shift ($\overline{\Delta z} = 0$) the waveguide with the 300 nm period, cannot effectively guide the wavelengths near $\lambda_0 = 1.55$ μm because it operates in the bandgap. In Figure 2b we show, with a dot for each shift, the Bragg wavelength movement with the shift estimated with the model proposed in the previous section by using Equation (5). Note that it only requires the Bragg wavelength of the non-bricked SWG structure $\lambda_B(\overline{\Delta z} = 0)$. This shortening of the Bragg wavelength is fundamental to achieving the desired metamaterial properties with a simple waveguide geometry with substantially increased pixel dimensions that enable wafer-scale fabrication.

3. Ultra-Broadband Beam Splitter with Large Pixel Dimensions

3.1. Design and Simulation

Dispersion and anisotropy control are key benefits enabled SWG metamaterials.[18] However, an optimization based only on tuning the period of the segments often yields fabrication resolutions about 100 nm and below,[19,20,24,27] hampering wafer-scale production of the chips. Our bricked SWGs offer an advantageous solution allowing engineering of optical metamaterial properties for substantially longer grating periods with correspondingly increased fabrication resolution. To show this

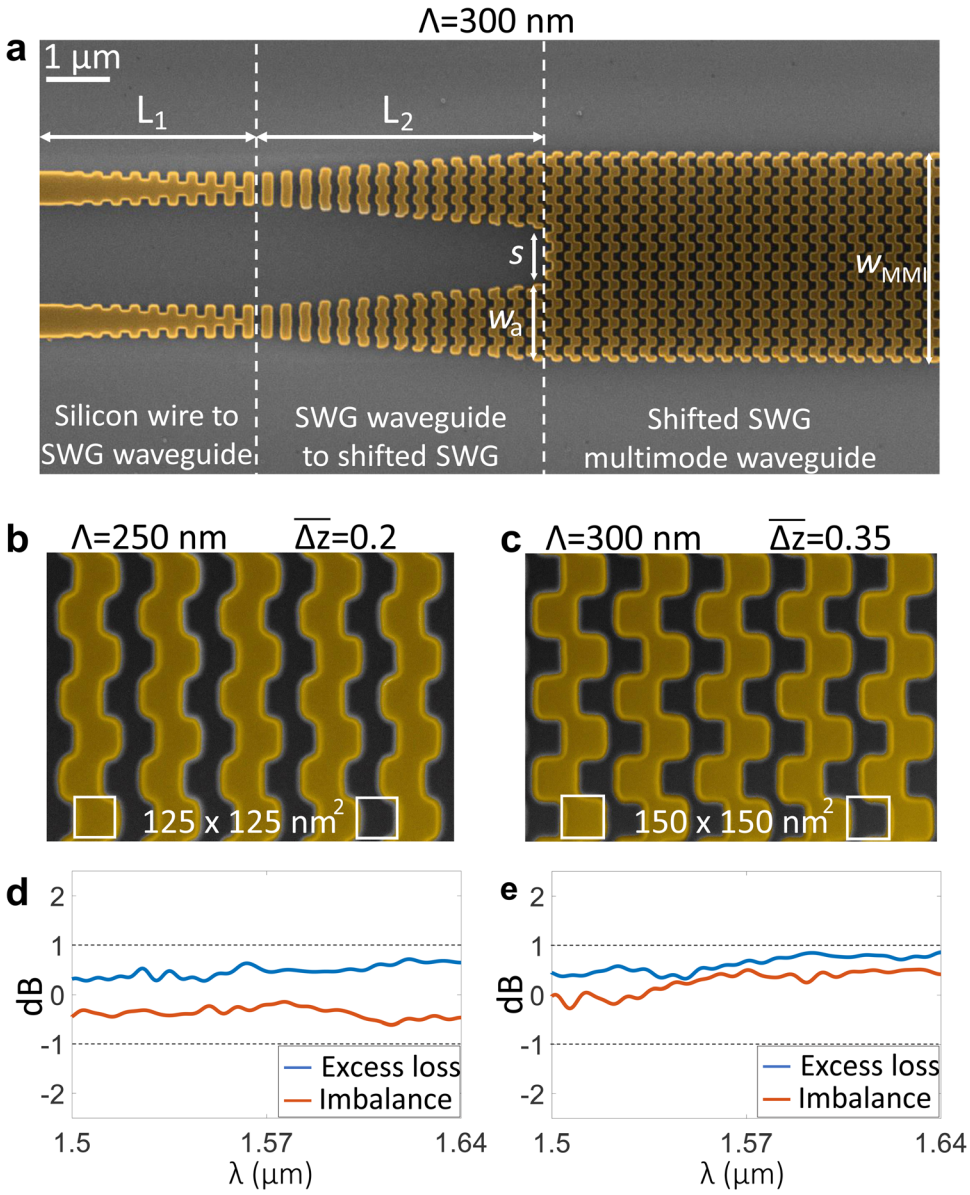

Figure 4. a) Scanning electron microscope (SEM) images of the input section of the bricked SWG MMI; $\Lambda_z = 300$ nm. Three different sections are shown: i) Transition from a silicon wire to a conventional SWG structure. ii) Transition from a conventional SWG structure to a bricked SWG topology. iii) Multimode bricked SWG waveguide. b,c) SEM image of the multimode region of the (b) $\Lambda = 250$ nm and (c) $\Lambda = 300$ nm structures. The square area of the silicon segments and the gaps in between is maintained constant independently of the shift $\overline{\Delta z}$ in both cases. d,e) Measured excess loss and imbalance for the (d) $\Lambda = 250$ nm and (e) $\Lambda = 300$ nm structures. In both cases the measured 1 dB bandwidth is limited to the 140 nm bandwidth of our setup.

capability, we use the 3.3 µm wide bricked SWG waveguides analyzed in the previous section to design two broadband 2 × 2 Multimode interferometers (MMI) couplers working for TE polarization, with SWG periods equal to $\Lambda = 250$ nm and $\Lambda = 300$ nm. MMIs have a remarkable practical interest, since they are widely used as a fundamental component in many photonic integrated devices, such as power splitters and combiners,[40] Mach–Zehnder interferometers (MZIs)[41] or 90° hybrids for coherent optical receivers.[42,43] Multimode interferometers replicate the input field into N separated output fields at certain propagation distance by means of the self-image principle.[44] In the general case, the distance where the input field is replicate N-times is given by the formula $L_{MMI} = 3L_\pi/N$, where L_π is the beat-length between the first and second modes, defined as

$$L_\pi(\lambda) = \frac{\lambda}{2\left(n_{eff1}(\lambda) - n_{eff2}(\lambda)\right)} \tag{6}$$

where η_{eff1} and η_{eff2} are the effective indices of the first and second TE Floquet-Bloch modes (see **Figure 3**a). Further details on MMI fundamentals and design can be found in the Supporting Information.

Table 1. Geometrical parameters of the bricked SWG MMIs.

Parameter	250 nm pitch design	300 nm pitch design
Silicon thickness (H)	220 nm	
MMI width (w_{MMI})	3.3 μm	
MMI length (L_{MMI})	16.5 μm	22.5 μm
Input width (w_a)	1.2 μm	
Si wire to SWG taper (L_1)	2.5 μm	3 μm
SWG to bricked SWG taper (L_2)	3.75 μm	4.5 μm
Input separation (s)	0.9 μm	
Period z (Λ_z)	250 nm	300 nm
Period x (Λ_x)	250 nm	300 nm
Shifting ($\overline{\Delta z}$)	0.2	0.35
Duty cycle z (DC_z)	50%	
Duty cycle x (DC_x)	50%	

The anisotropy and dispersion of SWG structures provide control over the beat-length, thereby shortening the device and achieving broadband behavior.[19] In Figure 3b,c we show the beat lengths with different shifts ranging from $\overline{\Delta z} = 0$ to $\overline{\Delta z} = 0.5$, for the $\Lambda = 250$ nm and $\Lambda = 300$ nm structures, respectively. It is observed that in both cases an almost flat beat length can be achieved for a shifting in-between the conventional, $\overline{\Delta z} = 0$, and the chequerboard type structure, $\overline{\Delta z} = 0.5$. Importantly, at the central wavelength of 1.55 μm, the $\Lambda = 300$ nm structure is in the bandgap when no shift is applied, and metamaterial operation allowing mode propagation is only enabled as the shift is increased. To control the modal excitation in the multimode waveguide, the input Si-wire waveguides are tapered as shown in **Figure 4**a. As can be seen in this figure, the tapers are divided in two sections: The first one is a conventional adiabatic taper from the Si-wire to an SWG waveguide ($\overline{\Delta z} = 0$) of the same width (w = 500 nm). The second section gradually transforms the SWG waveguide into the wider bricked SWG input port ($w_a = 1.2$ μm), which is done by linearly increasing the waveguide width while progressively introducing the shifting. This two-section taper is preferred to a direct conversion from the single-mode Si-wire to the widened bricked SWG structure since it minimizes losses arising from localized Bragg reflections. See the Supporting Information for further details on the two stage taper approach. The figures of merit used in the design of the MMI are the Excess Loss (EL) and the Imbalance (IB), defined as:

$$EL = -10\log(|S_{41}|^2 + |S_{31}|^2) \quad (7)$$

$$IB = 10\log(|S_{41}|^2/|S_{31}|^2) \quad (8)$$

where S_{31} and S_{41} are the scattering parameters which relate the power in the fundamental mode of the output waveguides with the power in the fundamental mode of the input port. The optimum shift for each design is fine-tuned with 3D-FDTD simulations of the full device, resulting in the optimum dimensions summarized in **Table 1** (see the Supporting Information for further details on the simulation approach). In Figure 3a we show the field propagation along the MMI for the 300 nm pitch device. In Figure 3d,e we show the calculated excess loss and imbalance of the optimized devices. Both designs show an ultra-broad bandwidth of 400 nm for an EL and IB lower than 1 dB with back reflections less than 16 dB over the full design bandwidth.

3.2. Experimental Results

To experimentally demonstrate our brick SWG design strategy, the devices were fabricated in a commercial silicon facility using e-beam patterning and experimentally characterized (see the Supporting Information for details). Scanning electron micrographs of the devices are shown in Figure 4a–c, with slight rounding of the rectangular geometry. As shown in Figure 4d,e the rounding had no significant impact on the performance of the devices, which both achieve EL and IB below 1 dB over the full 140 nm bandwidth of our laser. To the best of our knowledge this is the first time such outstanding performance is achieved with this large pixel sizes of 125 and 150 nm.

4. Conclusions

In this work we have demonstrated bricked SWG structures, a novel metamaterial topology that enables full lithographic control of permittivity tensor. The proposed topology relaxes the period limitations of traditional SWGs resulting in greater pixel dimensions which opens a new path toward wafer-scale fabrication of nanophotonic devices incorporating on-chip metamaterials. We have developed an analytical model that accurately predicts the behavior of the structure and have experimentally demonstrated a proof-of-concept 2×2 MMI nanophotonic coupler with bricked SWG metamaterial. Ultra-broad design bandwidth of 400 nm was confirmed by 3D FDTD simulations while our measurements reveal state-of-the-art performance over the full 140 nm bandwidth of our tunable laser, with pixel size dimensions as large as 150×150 nm^2. We believe that the unique advantages of bricked SWG topology will not only enable new silicon photonic devices with exceptional performance, but more importantly, will likely make the benefits of on-chip metamaterials available to the wider silicon photonics industry.

Supporting Information

Supporting Information is available from the Wiley Online Library or from the author.

Acknowledgements

The authors acknowledge funds from Universidad de Málaga, Ministerio de Economía y Competitividad (MINECO) (TEC2016-80718-R, PID2019-106747RB-I00), Ministerio de Educación, Cultura y Deporte (MECD) (FPU16/06762), Fondo Europeo de Desarrollo Regional—FEDER, Proyecto I+D+i en el marco del Programa Operativo FEDER Andalucía 2014–2020 (UMA18-FEDERJA-219) and Junta de Andalucía, Proyectos de Excelencia, Modalidad Retos (P18-RT-1453and P18-RT-793).

Conflict of Interest

The authors declare the following potential conflict of interest: This work is protected under Spanish patent No. P202030367.

Data Availability Statement

Research data will be shared upon reasonable request.

Keywords

anisotropy, integrated optics, multimode interference, silicon photonics, subwavelength grating metamaterials

Received: October 29, 2020
Revised: February 5, 2021
Published online: May 2, 2021

[1] P. Marin-Palomo, J. N. Kemal, M. Karpov, A. Kordts, J. Pfeifle, M. H. P. Pfeiffer, P. Trocha, S. Wolf, V. Brasch, M. H. Anderson, R. Rosenberger, K. Vijayan, W. Freude, T. J. Kippenberg, C. Koos, *Nature* **2017**, *546*, 274.
[2] J. Wang, S. Paesani, Y. Ding, R. Santagati, P. Skrzypczyk, A. Salavrakos, J. Tura, R. Augusiak, L. Mančinska, D. Bacco, D. Bonneau, J. W. Silverstone, Q. Gong, A. Acín, K. Rottwitt, L. K. Oxenløwe, J. L. O'Brien, A. Laing, M. G. Thompson, *Science* **2018**, *360*, 285.
[3] D. Llewellyn, Y. Ding, I. I. Faruque, S. Paesani, D. Bacco, R. Santagati, Y.-J. Qian, Y. Li, Y.-F. Xiao, M. Huber, M. Malik, G. F. Sinclair, X. Zhou, K. Rottwitt, J. L. O'Brien, J. G. Rarity, Q. Gong, L. K. Oxenlowe, J. Wang, M. G. Thompson, *Nat. Phys.* **2020**, *16*, 148.
[4] A. N. Tait, T. F. de Lima, E. Zhou, A. X. Wu, M. A. Nahmias, B. J. Shastri, P. R. Prucnal, *Sci. Rep.* **2017**, *7*, 7430.
[5] Y. Shen, N. C. Harris, S. Skirlo, M. Prabhu, T. Baehr-Jones, M. Hochberg, X. Sun, S. Zhao, H. Larochelle, D. Englund, M. Soljačić, *Nat. Photonics* **2017**, *11*, 441.
[6] C. Sun, M. T. Wade, Y. Lee, J. S. Orcutt, L. Alloatti, M. S. Georgas, A. S. Waterman, J. M. Shainline, R. R. Avizienis, S. Lin, B. R. Moss, R. Kumar, F. Pavanello, A. H. Atabaki, H. M. Cook, A. J. Ou, J. C. Leu, Y.-H. Chen, K. Asanović, R. J. Ram, M. A. Popović, V. M. Stojanović, *Nature* **2015**, *528*, 534.
[7] A. H. Atabaki, S. Moazeni, F. Pavanello, H. Gevorgyan, J. Notaros, L. Alloatti, M. T. Wade, C. Sun, S. A. Kruger, H. Meng, K. Al Qubaisi, I. Wang, B. Zhang, A. Khilo, C. V. Baiocco, M. A. Popović, V. M. Stojanović, R. J. Ram, *Nature* **2018**, *556*, 349.
[8] S. A. Miller, Y.-C. Chang, C. T. Phare, M. C. Shin, M. Zadka, S. P. Roberts, B. Stern, X. Ji, A. Mohanty, O. A. Jimenez Gordillo, U. D. Dave, M. Lipson, *Optica* **2020**, *7*, 3.
[9] E. Obrzud, M. Rainer, A. Harutyunyan, M. H. Anderson, J. Liu, M. Geiselmann, B. Chazelas, S. Kundermann, S. Lecomte, M. Cecconi, A. Ghedina, E. Molinari, F. Pepe, F. Wildi, F. Bouchy, T. J. Kippenberg, T. Herr, *Nat. Photonics* **2019**, *13*, 31.
[10] A. Fernández Gavela, D. Grajales García, J. Ramirez, L. Lechuga, *Sensors* **2016**, *16*, 285.
[11] K. Giewont, S. Hu, B. Peng, M. Rakowski, S. Rauch, J. C. Rosenberg, A. Sahin, I. Stobert, A. Stricker, K. Nummy, F. A. Anderson, J. Ayala, T. Barwicz, Y. Bian, K. K. Dezfulian, D. M. Gill, T. Houghton, *IEEE J. Sel. Top. Quantum Electron.* **2019**, *25*, 1.
[12] B. Szelag, K. Hassan, L. Adelmini, E. Ghegin, P. Rodriguez, F. Nemouchi, P. Brianceau, E. Vermande, A. Schembri, D. Carrara, P. Cavalie, F. Franchin, M.-C. Roure, L. Sanchez, C. Jany, S. Olivier, *IEEE J. Sel. Top. Quantum Electron.* **2019**, *25*, 1.
[13] P. Cheben, D.-X. Xu, S. Janz, A. Densmore, *Opt. Express* **2006**, *14*, 4695.
[14] P. Cheben, P. J. Bock, J. H. Schmid, J. Lapointe, S. Janz, D.-X. Xu, A. Densmore, A. Delâge, B. Lamontagne, T. J. Hall, *Opt. Lett.* **2010**, *35*, 2526.
[15] I. Staude, J. Schilling, *Nat. Photonics* **2017**, *11*, 274.
[16] P. Lalanne, P. Chavel, *Laser Photonics Rev.* **2017**, *11*, 1600295.
[17] R. Halir, A. Ortega-Moñux, D. Benedikovic, G. Z. Mashanovich, J. G. Wangüemert-Pérez, J. H. Schmid, Í. Molina-Fernández, P. Cheben, *Proc. IEEE* **2018**, *106*, 2144.
[18] P. Cheben, R. Halir, J. H. Schmid, H. A. Atwater, D. R. Smith, *Nature* **2018**, *560*, 565.
[19] R. Halir, P. Cheben, J. M. Luque-González, J. D. Sarmiento-Merenguel, J. H. Schmid, G. Wangüemert-Pérez, D.-X. Xu, S. Wang, A. Ortega-Moñux, Í. Molina-Fernández, *Laser Photonics Rev.* **2016**, *10*, 1039.
[20] D. González-Andrade, J. M. Luque-González, J. G. Wangüemert-Pérez, A. Ortega-Moñux, P. Cheben, Í. Molina-Fernández, A. V. Velasco, *Photonics Res.* **2020**, *8*, 359.
[21] R. Paniagua-Domínguez, Y. F. Yu, E. Khaidarov, S. Choi, V. Leong, R. M. Bakker, X. Liang, Y. H. Fu, V. Valuckas, L. A. Krivitsky, A. I. Kuznetsov, *Nano Lett.* **2018**, *18*, 2124.
[22] J. M. Luque-González, R. Halir, J. G. Wangüemert-Pérez, J. H. Schmid, P. Cheben, Í. Molina-Fernández, A. Ortega-Moñux, *Laser Photonics Rev.* **2019**, *13*, 1900172.
[23] Z. Wang, T. Li, A. Soman, D. Mao, T. Kananen, T. Gu, *Nat. Commun.* **2019**, *10*, 3547.
[24] S. Jahani, S. Kim, J. Atkinson, J. C. Wirth, F. Kalhor, A. Al Noman, W. D. Newman, P. Shekhar, K. Han, V. Van, R. G. DeCorby, L. Chrostowski, M. Qi, Z. Jacob, *Nat. Commun.* **2018**, *9*, 1893.
[25] B. Shen, P. Wang, R. Polson, R. Menon, *Nat. Photonics* **2015**, *9*, 378.
[26] A. Herrero-Bermello, J. M. Luque-Gonzalez, R. Halir, P. Cheben, A. Ortega-Moñux, Í. Molina-Fernández, A. V. Velasco, *IEEE Photonics J.* **2019**, *11*, 1.
[27] H. Xu, D. Dai, Y. Shi, *Laser Photonics Rev.* **2019**, *13*, 1800349.
[28] H. Xu, D. Dai, Y. Shi, *Photonics Res.* **2019**, *7*, 1432.
[29] J. M. Luque-González, A. Herrero-Bermello, A. Ortega-Moñux, M. Sánchez-Rodríguez, A. V. Velasco, J. H. Schmid, P. Cheben, Í. Molina-Fernández, R. Halir, *Opt. Lett.* **2020**, *45*, 3398.
[30] A. Herrero-Bermello, A. Dias-Ponte, J. M. Luque-González, A. Ortega-Moñux, A. V. Velasco, P. Cheben, R. Halir, *Opt. Express* **2020**, *28*, 16385.
[31] R. Gatdula, S. Abbaslou, M. Lu, A. Stein, W. Jiang, *Optica* **2019**, *6*, 585.
[32] E. Luan, H. Yun, L. Laplatine, Y. Dattner, D. M. Ratner, K. C. Cheung, L. Chrostowski, *IEEE J. Sel. Top. Quantum Electron.* **2019**, *25*, 1.
[33] L. Torrijos-Morán, A. Griol, J. García-Rupérez, *Opt. Lett.* **2019**, *44*, 4702.
[34] W. Lv, S. Liu, X. Wu, E. Y. Lam, *J. Opt. Soc. Am. A* **2014**, *31*, B19.
[35] J. M. Luque-González, A. Herrero-Bermello, A. Ortega-Moñux, Í. Molina-Fernández, A. V. Velasco, P. Cheben, J. H. Schmid, S. Wang, R. Halir, *Opt. Lett.* **2018**, *43*, 4691.
[36] S. M. Rytov, *Sov. Phys. JETP* **1956**, *2*, 466.
[37] P. Yeh, A. Yariv, C.-S. Hong, *J. Opt. Soc. Am.* **1977**, *67*, 423.
[38] J. Li, F. Miao, Z. Liang, S. Guenneau, *Opt. Express* **2015**, *23*, 7140.
[39] "BANDSOLVE Photonic band structure software," https://www.synopsys.com/photonic-solutions/rsoft-photonic-device-tools/passive-device-bandsolve.html (accessed: March 2018).
[40] A. Ortega-Moñux, C. Alonso-Ramos, A. Maese-Novo, R. Halir, L. Zavargo-Peche, D. Pérez-Galacho, I. Molina-Fernández, J. G. Wangüemert-Pérez, P. Cheben, J. H. Schmid, J. Lapointe, D. Xu, S. Janz, *Laser Photonics Rev.* **2013**, *7*, L12.
[41] D. J. Thomson, Y. Hu, G. T. Reed, J. Fedeli, *IEEE Photonics Technol. Lett.* **2010**, *22*, 1485.
[42] R. Halir, G. Roelkens, A. Ortega-Moñux, J. G. Wangüemert-Pérez, *Opt. Lett.* **2011**, *36*, 178.
[43] W. Yang, M. Yin, Y. Li, X. Wang, Z. Wang, *Opt. Express* **2013**, *21*, 28423.
[44] L. B. Soldano, E. C. M. Pennings, *J. Lightwave Technol.* **1995**, *13*, 615.